

Sonication-assisted synthesis of a strawberry-like nano-structure triphenyltin(IV) adduct as precursor for preparation of nano-sized SnP_2O_7 : Crystal structure and DFT calculations

Mahtab Alipour^a, Niloufar Dorosti^{a,*}, Maciej Kubicki^b

^a Department of Chemistry, Faculty of Science, Lorestan University, 68135-465, Khorramabad, Iran

^b Department of Chemistry, Adam Mickiewicz University, Uniwersytetu Poznańskiego 8, 61-614 Poznań, Poland

ARTICLE INFO

Article history:

Received 1 September 2020

Revised 26 October 2020

Accepted 9 November 2020

Available online 12 November 2020

Keywords:

Triorganotin

Crystal structure

Nanostrawberry

DFT calculations

Hirshfeld surface

ABSTRACT

A triphenyltin(IV) adduct of phosphoramidate with a formula of $[\text{Sn}(\text{Ph})_3\text{Cl}(\mathbf{L1})]$ (**C1**), **L1** = N-phenyl-N,N'-bis(pentamethylene) phosphoric triamide, has been synthesized and characterized by elemental analyses and IR spectroscopy. In the crystal structure, the tin(IV) environment adopts a distorted trigonal bipyramidal geometry with three phenyl groups in the equatorial plane, one chloro atom and the oxygen atom of ligand at the axial sites. Hirshfeld surface analysis and fingerprint plots were used to investigate the intermolecular interactions, responsible for the crystal architecture. The complex was also prepared under ultrasonic irradiation (**C1a**) and characterized by elemental analyses, IR, and X-ray powder diffraction (XRPD). The effects of two different concentrations of initial reagents on the size and morphology of the nanomaterial were studied by scanning electron microscopy (SEM), which shows that **C1a** grown as nano-strawberry morphology. The calcination of triorganotin complex in air atmosphere led to production of nano-structured tin pyrophosphate. The thermal stabilities of the single crystal and of the nano-crystalline form were investigated by thermal gravimetric and differential thermal analyses. The structural and electronic properties of **L1**, **C1** and similar molecules were evaluated by density functional theory (DFT) calculations. Parameters derived from NBO and QTAIM analyses suggest that the nature of Sn-O interaction is electrostatic with a small amount of covalent character and donor-acceptor delocalization from the ligand oxygen atom to the tin center. Moreover, the electronic parameters including HOMO-LUMO orbitals, bond gap, chemical hardness-softness, electronegativity, and electrophilicity were calculated.

© 2020 Elsevier B.V. All rights reserved.

1. Introduction

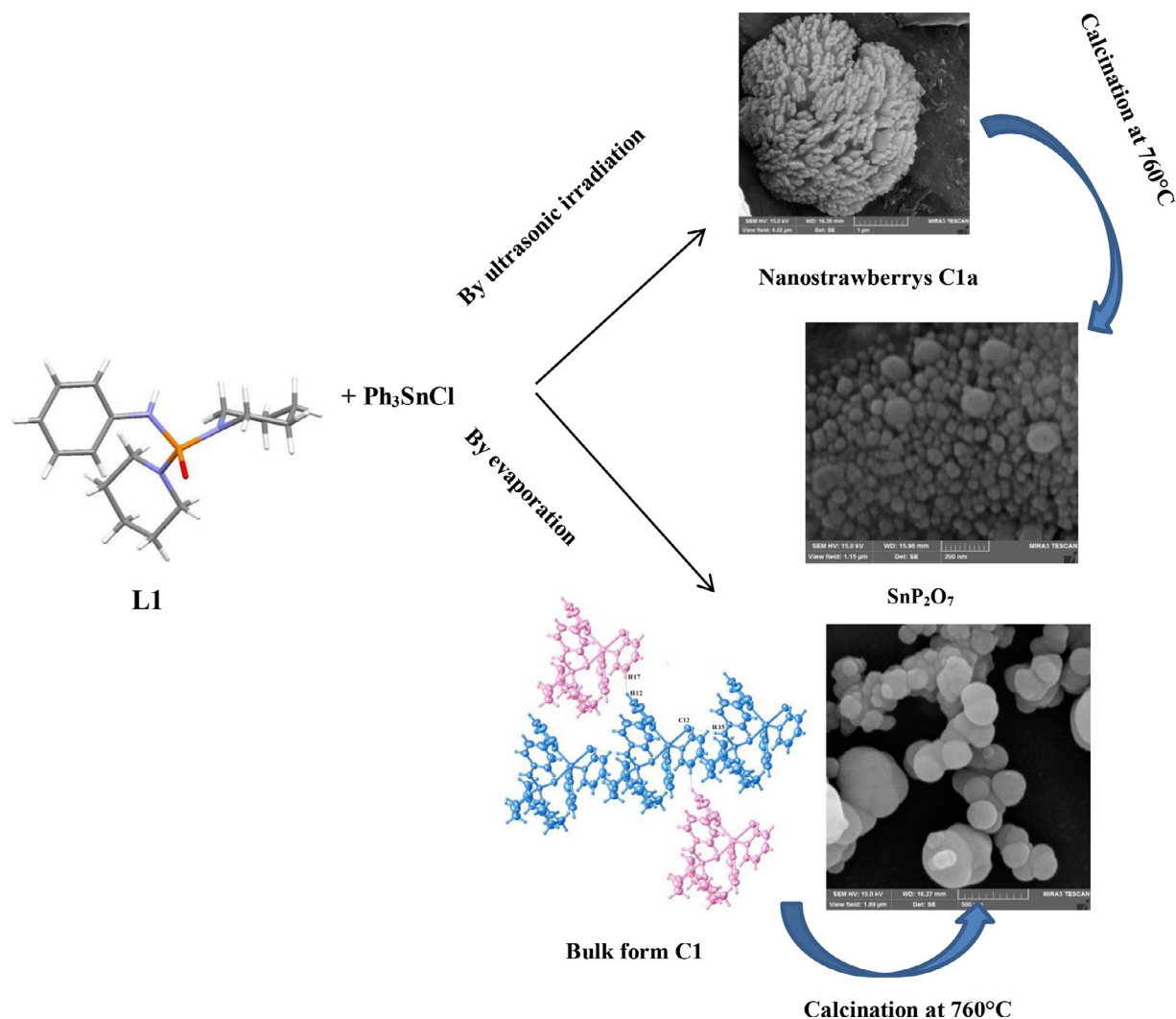
Organotin(IV) complexes have attracted continuous and increasing interest in coordination chemistry due to their different applications. They have been used, for instance, as efficient catalysts [1], biological agents [2], and agrochemical fungicides and biocides [3]. These materials also display many interesting nonlinear optical properties and therefore can be used in various photonic applications [4]. Coordination chemistry of organotin(IV) complexes with phosphoramidate ligands has frequently been studied and indicated six and five-coordinated structures [[5], [7]]. Nowadays, tin-phosphoramidate complexes have become the subject of diverse studies due to their antitumor [[6],[8]] and antibacterial [[7], [8]]

properties, as well as to their application as cholinesterase [9] inhibitors.

Preparation of nano-sized materials has been of particularly great interest due to the eminent properties which can be obtained at this scale, for instance large specific surface, which leads to the enhanced optical [10], electrical [11] and a plethora of medical applications [12]. In contrast to widely studied inorganic nanomaterials, the specific syntheses of metal coordination complexes at nano-scale seem to be surprisingly sparse, and to date most investigations on supramolecular coordination complexes have been carried out only in the solid-state and therefore the studies of their properties were limited to the investigations at the macroscopic scale. The potential use of supramolecular coordination complexes as materials for nanotechnological applications could be quite extensive, as the nanometer-scale materials often exhibit new and interesting size-dependent physical and chemical properties that cannot be observed in their bulk forms. For this reason, nano-size coordination complexes are interesting candidates for applica-

* Corresponding author.

E-mail address: dorosti.n@lu.ac.ir (N. Dorosti).



Scheme 1. Formation of bulk form (**C1**) and nanostrawberry (**C1a**) complex as well as the SnP_2O_7 particles obtained from their calcination at 760°C.

tions in many fields, including nonlinear optics [13], sensor [14], catalysis [15], magnetism, and molecular sensing [16]. Our research group has recently reported synthesis of some nano-size phosphoramidate-based tin(IV) complexes, which improves product biological activities [9, 17]. Additionally, SnP_2O_7 is an inorganic crystalline material with a possible usage as an anhydrous proton conductor in manufacturing fuel cells [18]. Despite the important role of tin pyrophosphate nanopowders in the fabrication of fuel cells, this compound was only prepared by coprecipitation method so far [19], and studies on the synthesis of its nanostructures have been lagging far behind. The use of organometallic compounds as precursors for preparing inorganic nano-materials has been investigated [20]. In our previous work, SnP_2O_7 nanopowders were synthesized by calcination method for the first time [21]. The size and morphology of these nanomaterials are the two significant properties, depending on the kind of selected precursors for the preparation of them, which play a key role in technological applications [22].

Continuing our previous works on the coordination chemistry of phosphoramidates with organotin compounds and studies on the relationship between the tin(IV)-phosphoramidates and the dimension of the resulting SnP_2O_7 nano-structure, we synthesized a novel five-coordinated triorganotin complex with the formula $[\text{Sn}(\text{Ph})_3\text{Cl}(\mathbf{L1})]$ (**L1**: N-phenyl-N,N'-bis(pentamethylene) phosphoric triamide [23]) at two different sizes (**C1** and **C1a**) by two differ-

ent methods (Scheme 1). Crystal structure of **C1** was determined by X-ray crystallography and demonstrated a distorted trigonal-bipyramidal geometry for Sn. An investigation of intermolecular interactions in **C1** via Hirshfeld surface analysis is also presented. Tin phosphate nanostructures have been fabricated from this tin(IV)-phosphoramidates by the calcination method and a thermal decomposition process.

On the other hand, the computational chemistry methods have become increasingly important as a supplement, if not a substitute, for the empirical methods in almost all areas of chemistry. Therefore, by using NBO and QTAIM analyses, we tried to get insight into the electronic aspects of interactions in some crystalline triorganotin (**C1-C3**), and into the nature of tin-ligand interaction.

2. Experimental

2.1. Materials and general methods

All chemicals were purchased and used without further purification. Infrared (IR) spectra were recorded on a Shimadzu FT-IR 8400S (Japan) with a temperature controlled high sensitivity detector (DLATGS detector) and a resolution of 4 cm^{-1} in the scan range $500\text{--}4000\text{ cm}^{-1}$ using KBr pellets. Elemental analysis was performed on a Heraeus CHN-O-RAPID analyzer. Melting points were measured on an Electrothermal 9100 apparatus. Electronic

spectra were recorded by Varian, Cary 100 UV-Vis spectrophotometer in the range of 200–800 nm. The ultrasonic bath unit (Elmasonic model P30H) with ultrasonic peak output 80 kHz and 100 W has been used for ultrasonic synthesis of the nanostructured complex. SEM images were obtained from a MIRA3 TESCAN field emission scanning electron microscope equipped with a link Energy-Dispersive X-ray (EDX) analyzer. The X-ray diffraction pattern of dry nanomaterial powder was obtained using an STOE STADIP diffractometer with monochromatized Cu K α radiation ($\lambda = 1.54 \text{ \AA}$). The simulated XRD powder pattern based on single-crystal data was prepared using Mercury software. Thermal decomposition behavior was measured with a Perkin LEMERS2 apparatus between 20 and 800°C in a static nitrogen atmosphere.

2.2. Crystal structure determination

Crystals suitable for X-ray crystallography were obtained from ethanol at room temperature. X-ray data of complex **C1** were collected on Rigaku Xcalibur four-circle diffractometer with EOS CCD detector and graphite-monochromated MoK α radiation ($\lambda=0.71073 \text{ \AA}$). The data were corrected for Lorentz-polarization as well as for absorption effects [24]. Precise unit-cell parameters were determined by a least-squares fit of 6213 reflections of the highest intensity, chosen from the whole experiment. The structure was solved with SHELXT [25] and refined with the full-matrix least-squares procedure on F² by SHELXL [1]. All non-hydrogen atoms were refined anisotropically. Hydrogen atoms were placed in idealized positions and refined as 'riding model' with isotropic displacement parameters set at 1.2 times U_{eq} of appropriate carrier atoms. The structure is disordered (one of the phenyl groups relative occupancies 0.65/0.35).

2.3. Computational details

Crystal Explorer 3.1 program [26] was used to perform the Hirshfeld surface analysis. The intermolecular interactions in the crystal structure **C1** are located and quantified using the dnorm map and the 2D fingerprint (FP) plots, respectively [1].

The X-ray structures were used as starting points for DFT calculations in the gas phase using the Gaussian 09 suite of programs [27]. Since X-ray crystallography cannot locate accurately the position of the hydrogen atoms, optimization of the hydrogen atoms positions is needed for the X-ray structures. The structures (**L1-L3**; **C1-C3**) were fully optimized using B3LYP [28]. Non-metal atoms H, C, N, O, P and Cl were described by the standard basis set 6-311+G*, but LanL2DZ [29] was used for Sn atom. Quantum theory of atoms in molecules (QTAIM) [30], and natural bond orbital (NBO) [31] analyses were performed at the B3LYP/LANL2DZ/6-311+G* level of theory to evaluate the electronic structure of these molecules. The HOMO - LUMO energies and related parameters such as electronegativity, chemical hardness and softness for the selected compounds were calculated at the title level.

2.4. Synthesis

2.4.1. Synthesis of N-phenyl-N,N'-bis(pentamethylene) phosphoric triamide (**L1**)

The ligand (**L1**) was prepared and purified according to the literature procedure [23]. To a stirred solution of N-phenyl phosphoramidic dichloride (1 mmol, 0.209 g) in dry acetonitrile, piperidine (4 mmol, 0.341 g) was added dropwise at 0°C and the mixture stirred for 5 h. Then the solution was evaporated and the resulting white precipitate was washed with distilled water.

M.p. 129–130°C. IR (KBr, cm⁻¹): 3157 (m, NH), 3051 (w), 2931 (m, CH), 2845 (w), 1745 (s, C=C), 1601 (m), 1497 (s), 1448 (m), 1413 (m), 1335 (m), 1288 (m), 1213 (s), 1165 (s, P=O), 1119 (m),

1070 (s), 1032 (m), 957 (s), 926 (s, P-N), 845 (m), 804 (m), 752 (s, P-N), 735 (s), 690 (s), 611 (m), 552 (m), 502 (m), 469 (m). UV-Vis in ethanol: $\lambda_{\text{max}} = 229 \text{ nm} (\pi \rightarrow \pi^*)$, 280 nm ($n \rightarrow \pi^*$).

2.4.2. Synthesis of [N-phenyl-N,N'-bis(pentamethylene) phosphoric triamide] chloro triphenyltin(IV) (**C1**) by evaporation method

To a solution of ligand (0.5 mmol, 0.154 g) in 20 mL methanol, triphenyltin(IV) chloride (0.5 mmol, 0.193 g) was added and heated (60–70°C) for a few hours and the resulting mixture was then stirred at room temperature overnight. The obtained solid white material was filtered and washed several times with methanol. Suitable single crystals of **C1** were obtained by recrystallization from ethanol solution at room temperature.

Yield 45%, M.p. 229–230°C; Anal. Calc. for C₃₄H₄₁ClN₃OPSn: C, 58.94; H, 5.96; N, 6.06%. Found: C, 58.87; H, 5.90; N, 6.21%. IR (KBr, cm⁻¹): 3269 (m, NH), 3058 (w), 2941 (m, CH), 2849 (w), 1745 (s, C=C), 1603 (m), 1493 (m), 1371 (w), 1337 (m), 1292 (s), 1209 (w), 1145 (s, P=O), 1072 (s), 1028 (w), 955 (s, P-N), 847 (w), 798 (w), 735 (s, P-N), 694 (s), 609 (w), 544 (w, Sn-C), 507 (m), 451(s), 449 (m, Sn-O). UV-Vis in ethanol: $\lambda_{\text{max}} = 229 \text{ nm} (\pi \rightarrow \pi^*)$, 280 nm ($n \rightarrow \pi^*$).

2.4.3. Synthesis of nanostrawberry [N-phenyl- N,N'-bis(pentamethylene) phosphoric triamide] chloro triphenyltin(IV) by a sonochemical process (**C1a**)

5 mL solution of N-phenyl-N,N'-bis(pentamethylene) phosphoric triamide (**L1**) (0.007 mmol, 0.0022 g) in ethanol was positioned in an ultrasonic bath, operating at 80 kHz and 100 W. Into this ethanolic solution, a 5 mL solution of (C₆H₅)₃SnCl (0.007 mmol, 0.0027 g) in ethanol was added dropwise. After the end of the titration, the solution was kept in the bath for a selected aging time at ambient temperature. The obtained precipitates were filtered off, subsequently washed with ethanol and then dried in air.

Yield 37%, M.p. 228–230°C; Anal. Calc. for C₃₄H₄₁ClN₃OPSn: C, 58.94; H, 5.96; N, 6.06%. Found: C, 58.90; H, 6.01; N, 6.10%. IR (KBr, cm⁻¹): 3263 (m, NH), 3053 (w), 2939 (m, CH), 2849 (w), 1745 (s, C=C), 1606 (m), 1493 (m), 1371 (w), 1335 (m), 1286 (s), 1209 (w), 1145 (s, P=O), 1070 (s), 1028 (w), 953 (s, P-N), 847 (w), 793 (w), 735 (s, P-N), 692 (m), 615 (w), 544 (w, Sn-C), 502 (w), 455 (s), 449 (m, Sn-O). UV-Vis in ethanol: $\lambda_{\text{max}} = 229 \text{ nm} (\pi \rightarrow \pi^*)$, 280 nm ($n \rightarrow \pi^*$).

2.4.4. Preparation of SnP₂O₇ nanomaterial

To fabricate tin pyrophosphate nano-structures, the 0.073 g of tin(IV)-phosphoric triamide complex at two different sizes, **C1** and **C1a**, was calcinated at 760°C in a furnace in air and without any surfactant for 4 h. The SnP₂O₇ nanomaterials were obtained at this thermal treating.

3. Results and discussion

Scheme 1 shows the reaction between triphenyltinchloride and N-phenyl-N,N'-bis(pentamethylene) phosphoric triamide (**L1**) by two different methods and their conversion to nano-structured tin pyrophosphate by calcination at 760°C. The reaction between ligand (**L1**) and SnPh₃Cl provided a crystalline material of the formula Sn(Ph)₃Cl[C₆H₅NHP(O)(NC₅H₁₀)₂] (**C1**). The IR spectra indicate that the $\nu(\text{P=O})$ value decreases from **L1** (1165 cm⁻¹) to **C1** (1145 cm⁻¹), exhibiting the weakening of the P=O bond. Also, the $\nu(\text{P-N})$ increases from 926 cm⁻¹ (in **L1**) to 955 cm⁻¹ (in **C1**) that is due to the enhanced interaction of phosphorus atom with nitrogen lone pair to form a stronger, partial multiple bond. Other prominent band at 3157 cm⁻¹ is assigned to N-H vibrational mode that shifts toward higher frequencies in the coordinated ligand (3269 cm⁻¹). Whereas the N-H bond participates in the hydrogen bonding, the positive shift of $\nu(\text{N-H})$ may be attributed to the weakening of the hydrogen bond from NH...O_{P=O} ($d_{\text{N...O}} = 3.000 \text{ \AA}$) in **L1**

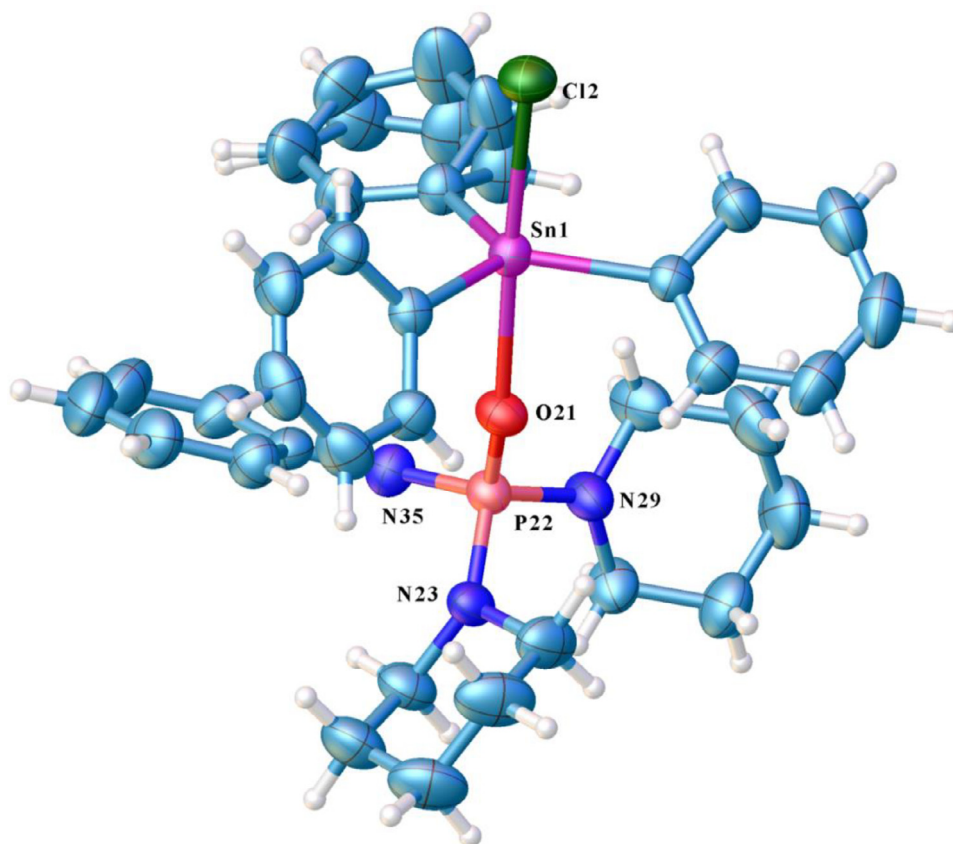


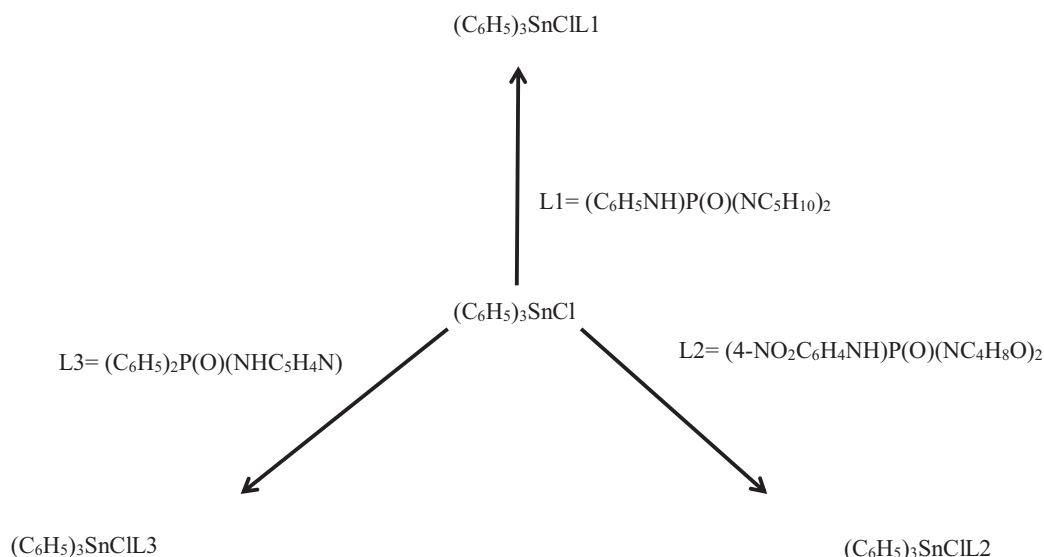
Fig. 1. The ORTEP diagram of **C1**. Ellipsoids are drawn at the 50% probability level.

[23] to $\text{NH}\dots\text{Cl}$ ($d_{\text{N}\dots\text{Cl}} = 3.451 \text{ \AA}$) in **C1**, which was confirmed by the X-ray crystallographic structures.

In order to check prevailing coordination modes, various molar ratios of ligand to SnPh_3Cl were assessed in the crystallization. The crystals of the five-coordinated complex **C1** grew from a sample of 2:1 ligand-to- Ph_3SnCl ratio, therefore, we may guess that the formation of **C1** is rather driven by the steric and electronic features of the ligand **L1**, and is independent of the molar ratio. Selected spectroscopic data of **C1** are listed in Table S1. The ORTEP view of **C1** is represented in Fig. 1 as well. The coordination polyhedron of tin can be described as distorted trigonal bipyramidal, with three phenyl groups [$\text{Sn}(1)\text{-C}(9)$, $2.124(2)$; $\text{Sn}(1)\text{-C}(3)$, $2.135(2)$ and $\text{Sn}(1)\text{-C}(15)$, $2.137(2) \text{ \AA}$] in the equatorial plane, chloro atom ($\text{Sn}(1)\text{-Cl}(2)$, $2.550(6) \text{ \AA}$) and the phosphoryl oxygen atom ($\text{Sn}(1)\text{-O}(21)$, $2.297(14) \text{ \AA}$) at the axial sites. The trans angle around tin, $\text{Cl}2\text{-Sn}1\text{-O}21$, is $177.59(4)^\circ$, so it deviates only slightly from linearity, and the sum of angles in the trigonal girdle around Sn are 359.4° . The Sn-C and Sn-Cl bond lengths are in the range of the covalent bond [32], while the Sn-O bond length is typical for the coordinate bond [33]. The P=O bond length in molecule **C1** is $1.486(15) \text{ \AA}$ that is larger than the normal P=O bond length (1.45 \AA) [34]. The P atom has slightly distorted tetrahedral configuration, with the surrounding angles around the P atoms in the range of $106.80(10) - 112.73(9)^\circ$. The P-N bonds ($1.645(2)\text{-}1.654(3) \text{ \AA}$ in **L1** and $1.626(19)\text{-}1.646(18) \text{ \AA}$ in **C1**) are shorter than the typical P-N single bond length (1.77 \AA) [34]. Selected structural data for **C1**, similar complexes containing $(\text{C}_6\text{H}_5)_3(\text{Cl})\text{Sn-O=P-}$ moiety [[35], [36]] and their corresponding phosphoramides (**L1** - **L3**) (Scheme 2) are presented in Table 1. It is seen from the table that the Sn-O, P=O, and P-N bond lengths are in the range of $2.297(14)\text{-}2.464(15) \text{ \AA}$, $1.483(18)\text{-}1.489(15) \text{ \AA}$ and $1.626(19)\text{-}1.686(7) \text{ \AA}$, respectively. The O-P-N_(aniline) bond an-

gles are nearly tetrahedral that range from $107.9(3)^\circ$ to $116.45(13)^\circ$, while P-N_(aniline)-C bond angles are deviate slightly from the idealized value, 120° , range from $118.6(2)^\circ$ to $128.8(2)^\circ$. The presence of Sn-Cl group in complex **C1** leads to the formation of intermolecular N(35)H(35)...Cl2 classical hydrogen bonds, which build up 1D chains of tin(IV) adducts and the free ligand expanding along [100] direction (Fig. 2a). The presence of short contacts as H...H and C...H results in a 2D network (Fig. 2b).

We used the Hirshfeld surface analysis to explore the intermolecular interactions [37] in a molecular crystal of **C1**. The Hirshfeld surfaces mapped with the normalized contact distance, d_{norm} , range -1.0 to 1.0 \AA , and full fingerprint plots were generated by means of the program Crystal Explorer 3.0 [38]. d_{norm} is displayed using a red-white-blue color scheme, and its value is negative (red regions) and positive (blue regions) for contacts shorter and longer than van der Waals separations, respectively. Fingerprint plots, constructed by plotting d_e against d_i (d_e and d_i are defined as distances from the surface to the nearest nucleus exterior and interior to the surface, respectively) simultaneously summarize the information from the intermolecular interactions present in molecular crystals into a two-dimensional colored plot. On the Hirshfeld surfaces (d_{norm}) of **C1** (Fig. 3a), one deep red area and one light red spot, labeled as 1 and 2, display the intermolecular N-H...Cl interactions as well as C-H...H-C weak interaction, respectively. On the two-dimensional fingerprint plots of **C1**, the N-H...Cl contacts appear as two long sharp spikes, comprising 9.1% of the total Hirshfeld surface area of the molecule (Fig. 3b, top-right). The upper spike (where $d_e > d_i$) corresponds to the hydrogen-bond donor (labeled as 1a), and the lower spike (where $d_e < d_i$) corresponds to the hydrogen-bond acceptor (labeled as 1b), with $d_e + d_i \sim 2.4 \text{ \AA}$. Moreover, the proportion of H...H and C...H short contacts is quantified as 72.6% and 18.3%, respectively (Fig. 3b, bottom-right and bottom-



Scheme 2. The structure of some complexes containing moiety $(C_6H_5)_3SnCl$ and their corresponding ligands.

Table 1
Selected structural data for compounds **L1**, **L2**, **C1–C3**.

Compound	Crystal system, Space group	Sn–O	P=O	P–N	O–P–N	P–N–C	Ref
L1	Triclinic, $P\bar{1}$	-	1.486(2)	1.644(3) 1.644(2)	116.45(13) 110.94(12) 109.79(12)	128.8(2) 124.7(2), 118.6(2) 118.6(2), 119.0(2)	[22]
L2	Monoclinic, $P2_1/n$	-	1.476(11)	1.657(12) 1.638(12) 1.647(12)	113.49(6) 111.52(6) 111.14(6)	127.27(10) 120.00(9), 125.69(9) 117.95(10), 122.17(9)	[35]
$[Sn(C_6H_5)_3ClL1]$ (C1)	Triclinic, $P\bar{1}$	2.297(14)	1.486(15)	1.646(18) 1.626(19) 1.634(19)	112.73(9) 110.51(9) 110.46(9)	128.63(15) 122.27(16), 121.79(16) 125.54(16), 119.01(16)	This work
$[Sn(C_6H_5)_3ClL2]$ (C2)	Monoclinic, $P2_1/n$	2.313(14)	1.483(18)	1.651(2) 1.686(7) 1.635(14)	113.22(9) 107.9(3) 111.9(6)	127.95(19) 126.5(7), 120.2(6) 125.6(12), 119.3(11)	[35]
$[Sn(C_6H_5)_3ClL3]$ (C3)	Monoclinic, $C2/c$	2.464(15)	1.489(15)	1.666(18)	114.26(9)	124.93(15)	[36]

L1: $(C_6H_5NH)P(O)(NC_5H_{10})_2$; **L2:** $(4-NO_2C_6H_4NH)P(O)(NC_4H_8O)_2$; **L3:** $(C_6H_5)_2P(O)(NHC_5H_4N)$.

left). This analysis shows the major influence of the H...H short contacts in the 2D network.

Spectral studies of nanostrawberry [N-phenyl- N, N'-bis(pentamethylene) phosphoric triamide] chloro triphenyltin (IV)

The elemental analysis, IR and UV–Vis spectra of the nanostructure (denoted by **C1a**) and of the single crystalline material are indistinguishable. The medium IR absorption bands around 3269–3263 cm^{-1} are assigned to N–H modes and the C–H modes involving the aliphatic ring hydrogen atoms produce a band at around 2940 cm^{-1} (Fig. 4). The absorption band near 1493 cm^{-1} corresponds to ring vibrations of the phenyl moiety, and vibrations of the phosphoryl group are observed around 1145 cm^{-1} . The band at about 544 cm^{-1} corresponds to stretching frequency of Sn–C bonds as well as the medium band at 449 cm^{-1} is assigned to the Sn–O stretching mode.

Figure S1 shows the UV–Vis spectrum of the tin(IV) complexes (**C1** and **C1a**) dissolved in ethanol. The absorption bands in the UV region are observed at wavelengths of about 229 and 280 nm, which can be attributed to the interligand $\pi \rightarrow \pi^*$ and $n \rightarrow \pi^*$ transitions [[21], [39]]. It is clearly seen that the UV–Vis spectrum of the complex is very similar for both scales.

Fig. 5 shows the simulated XRD pattern from single crystal X-ray data of compound **C1** compared to the XRD pattern of a typical sample of **C1** and **C1a** prepared by the evaporation process and sonochemical method, respectively. Acceptable matches, with slight differences in 2θ , were observed between the simulated and the experimental powder X-ray diffraction patterns (Fig. 5a–c), which indicate the same single crystalline phases for the compound obtained by both two methods. The formation of materials with small size could only happen when the concentration of initial reagents is within a suitable range for nucleation. The mor-

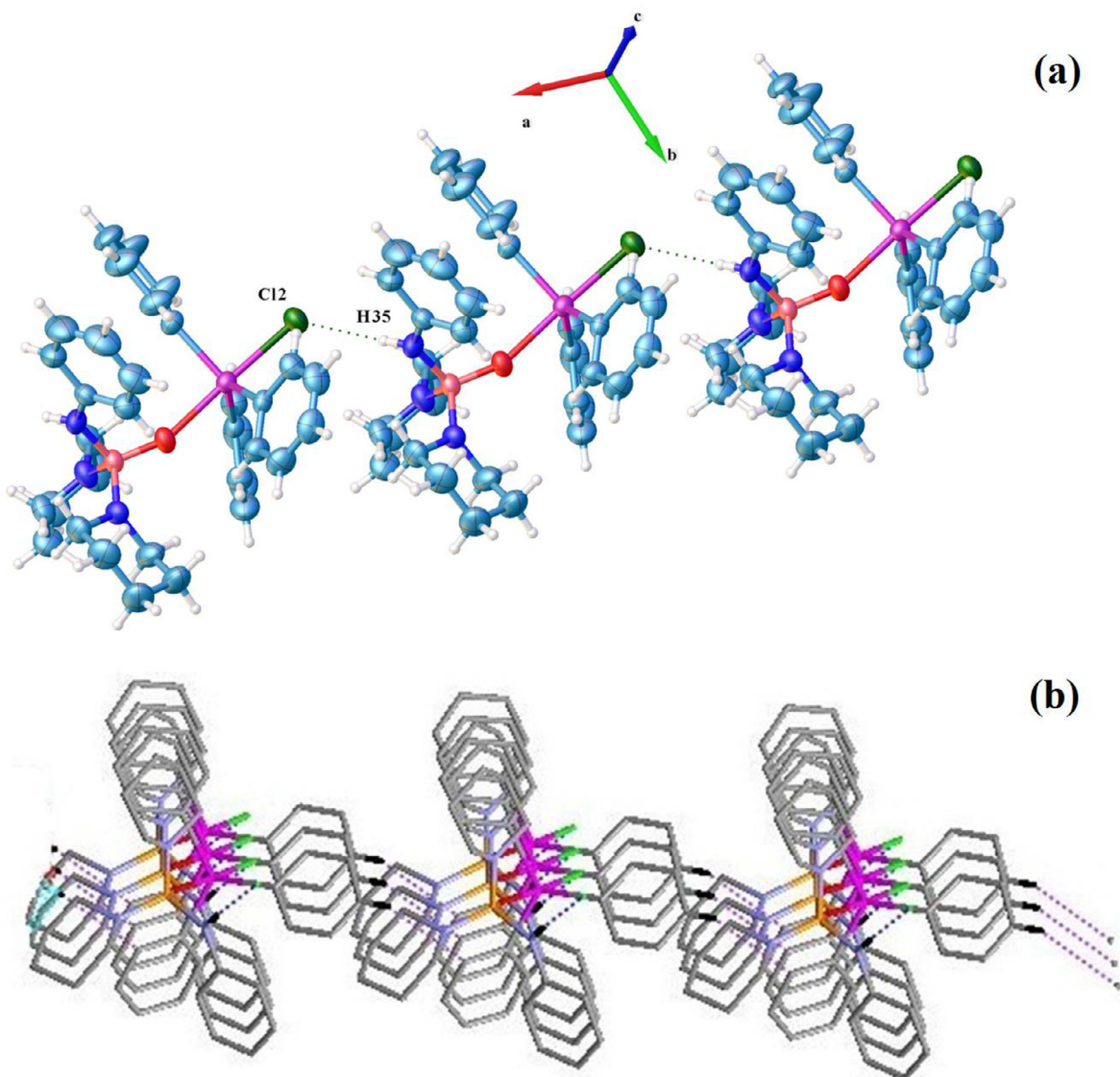


Fig. 2. (a) Representation of dimeric units in **C1** and the association of them through NH...Cl interactions, creating 1D chains along [100] direction; (b) Side view of the crystal packing, which show connection of 1D chains through short contacts H...H and C...H in 2D network.

Table 2

Calculated natural charges, second order stabilization energies between donor and acceptor orbitals ($E^{(2)}$, kcal/mol), natural electron configuration (NEC), hybridization of O lone pairs in $P=O$ bond, and Wiberg bond indices of Sn-O and P=O in the studied molecules.

Compound	Atomic Charge		$E^{(2)}$	NEC		Hybridization		WBI	
	$q(\text{Sn})$	$q(\text{O}_{\text{P=O}})$		$\text{O}_{\text{P=O}}$	O in P=O	LP of (O)	Sn-O	P=O	
L1	-	-1.09	-	[Core]2S ^{1.80} 2p ^{5.28}	Sp ^{2.28} d ^{0.05}	LP(1) Sp ^{0.5} LP(2) Sp ^{1.00} LP(3) Sp ^{1.00}			
L2	-	-1.08	-	[Core]2S ^{1.80} 2p ^{5.27}	Sp ^{1.8} 1	LP(1) Sp ^{0.55} LP(2) Sp ^{1.00} LP(3) Sp ^{1.00}			
L3	-	-1.07	-	[Core]2S ^{1.80} 2p ^{5.25}	Sp ^{1.87}	LP(1) Sp ^{0.51} LP(2) Sp ^{1.00} LP(3) Sp ^{0.99} d ^{0.70}			
[Sn(C ₆ H ₅) ₃ ClL1] (C1)	2.170	-1.14	29.50	[Core]2S ^{1.77} 2p ^{5.36}	Sp ^{1.61}	LP(1) Sp ^{0.63} LP(2) Sp ^{0.99} d ^{0.11} LP(3) Sp ^{0.99} d ^{0.52}	0.1431	1.0848	
[Sn(C ₆ H ₅) ₃ ClL2] (C2)	2.158	-1.12	24.77	[Core] 2S ^{1.77} 2p ^{5.34}	Sp ^{1.66}	LP(1) Sp ^{0.61} LP(2) Sp ^{0.99} d ^{0.61} LP(3) Sp ^{1.00}	0.1154	1.1266	
[Sn(C ₆ H ₅) ₃ ClL3] (C3)	2.091	-1.13	26.28	[Core]2S ^{1.76} 2p ^{5.36} 3p ^{0.01}	Sp ^{1.87}	LP(1)Sp ^{0.59} LP(2)Sp ^{0.99} d ^{0.07} LP(3)Sp ^{0.87} 1d ^{0.04}	0.1409	1.0810	

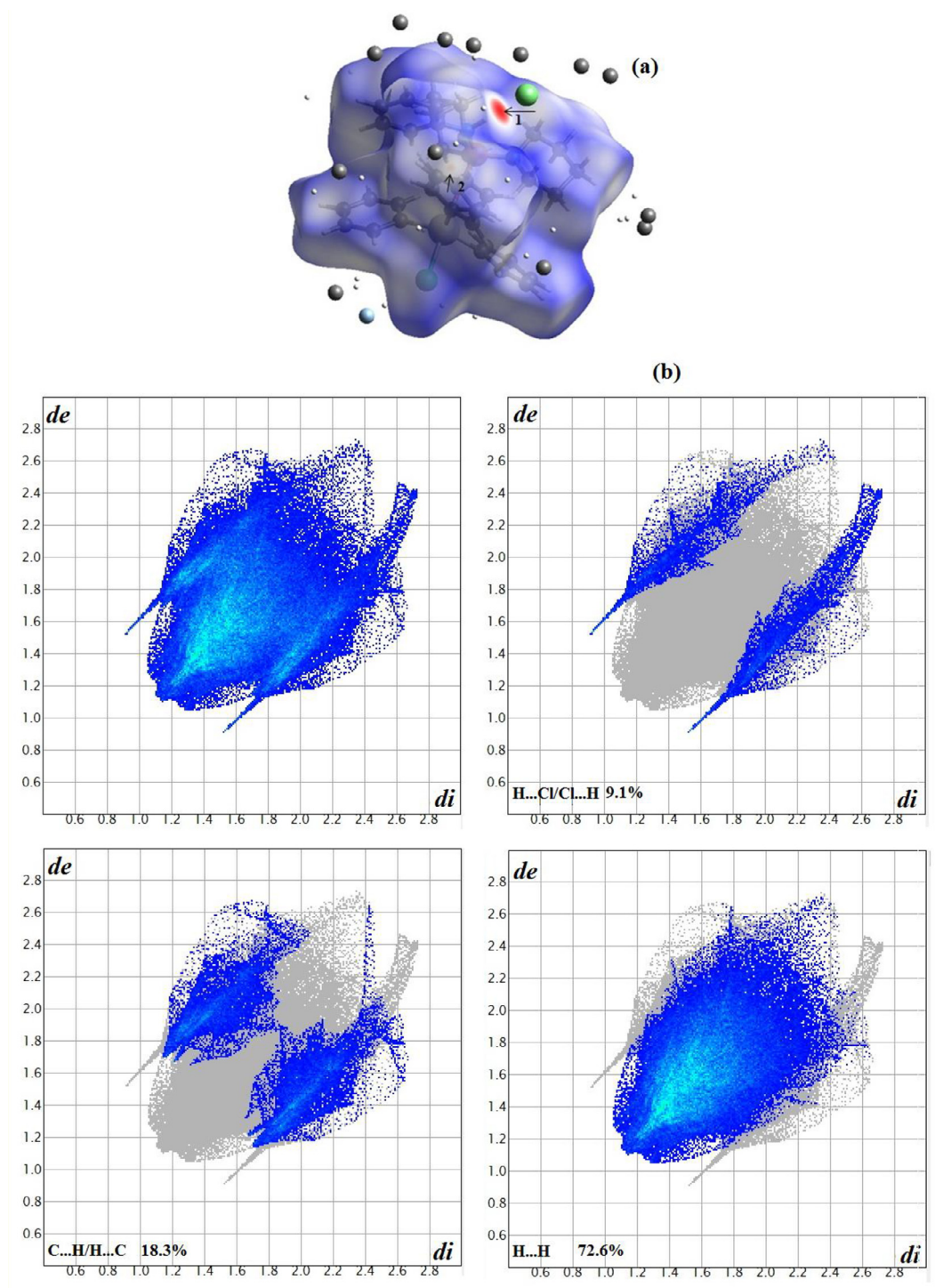


Fig. 3. Hirshfeld surfaces mapped with (a) d_{norm} of **C1** and (b) 2D fingerprint plots, full and resolved into HCl/ClH, CH/HC and H/H contacts showing percentages of contacts contributed to the total Hirshfeld surface area of molecule.

phology and size of **C1a**, for two samples which were prepared by the sonochemical process, were investigated by means of scanning electron microscopy (SEM). As could be observed, concentration decrease from 0.01 mM (Fig. 6a) to 0.007 mM (Fig. 6b) results in the formation of the smaller nano-structure. In our previous papers, we reported triorganotin-phosphoramides with a rod morphology at nano and micro scale [[21,39]]. Here, the morphology of **C1a** prepared by the sonochemical method is very interesting. It is composed of rods with diameters between 50 and 70 nm and the length varying between 188 and 360 nm, so arranged as to form

a strawberry network (Fig. 6b). Additionally, the chemical purity and stoichiometry of **C1a** were verified by EDX analysis. The EDX spectra in Fig. S2(a) confirm the presence of C, N, O, P, Cl, and Sn elements in the nano-structured of **C1a** with weight percentages of 57.37%, 18.33%, 21.72%, 1.23%, 0.79%, and 0.56%, respectively. The elemental mapping of nano powders **C1a** is presented in Fig. S2(b). In these images, the uniform distribution of the elements was observed throughout the sample, which confirmed the formation of tin-phosphoric triamide NPs (**C1a**).

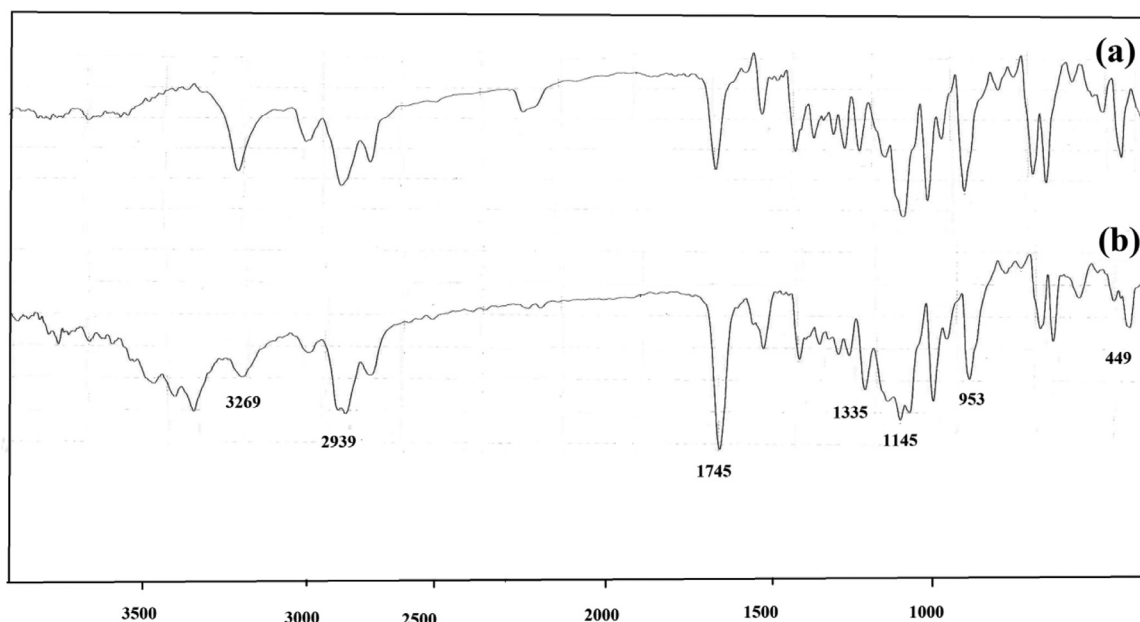


Fig. 4. IR spectra of (a) bulk material of **C1** and (b) nano-structure of **C1a**.

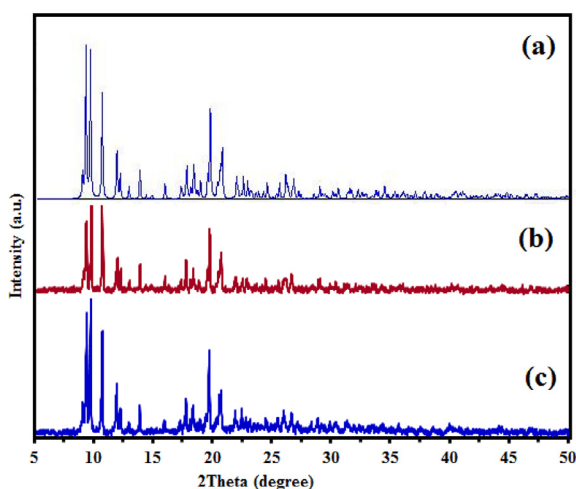


Fig. 5. The XRD patterns of (a) simulated from single crystal X-ray data of complex **C1**; (b) single crystal of **C1** and (c) nano-structure of **C1a**.

The thermogravimetry and differential thermal analysis (TGA and DTA) were carried out in flowing nitrogen at the heating rate of 10 °C/min (Fig. 7a). The thermogram of the nano-structures **C1a** indicates that the complex is thermally stable up to nearly 195 °C. Decomposition of **C1a** occurs between 195 and 273 °C in one step with a mass loss of 70% (calc. 74.1%) so that the organic segments including phenyl, pentamethylene rings as well as aniline and chlorine groups are eliminated in the same decomposition step. The result suggests that there is no coordination water in the complex. Also, the DTA curve shows an endothermic peak at 203 °C corresponding to a sharp weight loss in the TG curve; it proves that the complex undergoes decomposition.

The use of organotinphosphoric triamides as precursors for preparing tin pyrophosphate nano-materials has not yet been investigated thoroughly; hence, based on our knowledge, these compounds were synthesized by calcination of nano-tin phosphoramidate complexes in our laboratory for the first time [39]. It seems that the kind of precursor can change the morphology, size and type of SnP₂O₇ phase. Then, bulk form (**C1**) and nanoscale (**C1a**)

calculated at 760 °C in air and without any surfactant or capping molecule. The final product obtained upon calcinations of the title compound is, based on their XRD patterns, cubic SnP₂O₇, in perfect agreement with the results of EDS (Table S2). The phase purity of the prepared cubic SnP₂O₇ nano-powders is completely obvious and all diffraction peaks are perfectly indexed to the cubic SnP₂O₇ structure with the cell parameters of $a = b = c = 7.95 \text{ \AA}$, $\alpha = \beta = \gamma = 90^\circ$, $Z = 4$ and S.G = Pa3 (JCPDS card file No. 03-0287). No characteristic peaks of impurities are detected in the XRD pattern (Fig. S3). The SEM image and the corresponding particle size distribution histogram of the residue obtained from the calcination of **C1** and **C1a** at 760 °C under air atmosphere show that the particles are spherical, but ranging from 20 to 60 nm in size with the frequency of 30–40 nm at diameter for **C1a** (Fig. 8a, b).

3.1. Quantum chemical calculations

The optimized structures of the complex **C1** were obtained at the B3LYP and cam-B3LYP methods with LANL2DZ/6-311G* level basis set. Similar geometric parameters are obtained by the two applied methods, some of the calculated bond lengths and bond angles are included in Table S3. Although the biggest differences between calculated and experimental values of bond lengths and angles are about 0.080 Å, 0.063 Å and 4.77°, 6.66° for B3LYP and cam-B3LYP methods, respectively, the results obtained by the B3LYP method at 6-311G**/LANL2DZ correlate slightly better for **C1**. Subsequently, NBO, QTAIM, and Wiberg index analyses were performed to obtain more information about bonding and electronic aspects for the new synthesized complex, similar triorganotin(IV) and the corresponding ligands. By QM calculations, HOMO-LUMO energy gap was calculated as well.

3.2. NBO analysis

The electronic data of some triorganotin(IV) complexes (**C1** - **C3**) all containing (C₆H₅)₃ClSn-O=P moiety and their corresponding phosphoramidates (**L1** - **L3**) are presented in Table 2. In the phosphoramidate **L1**, the negative charge localized on O_{P=O} atom is larger in magnitude due to the nature of the substituents on phosphoryl, and the hybridization of occupied orbitals by the lone

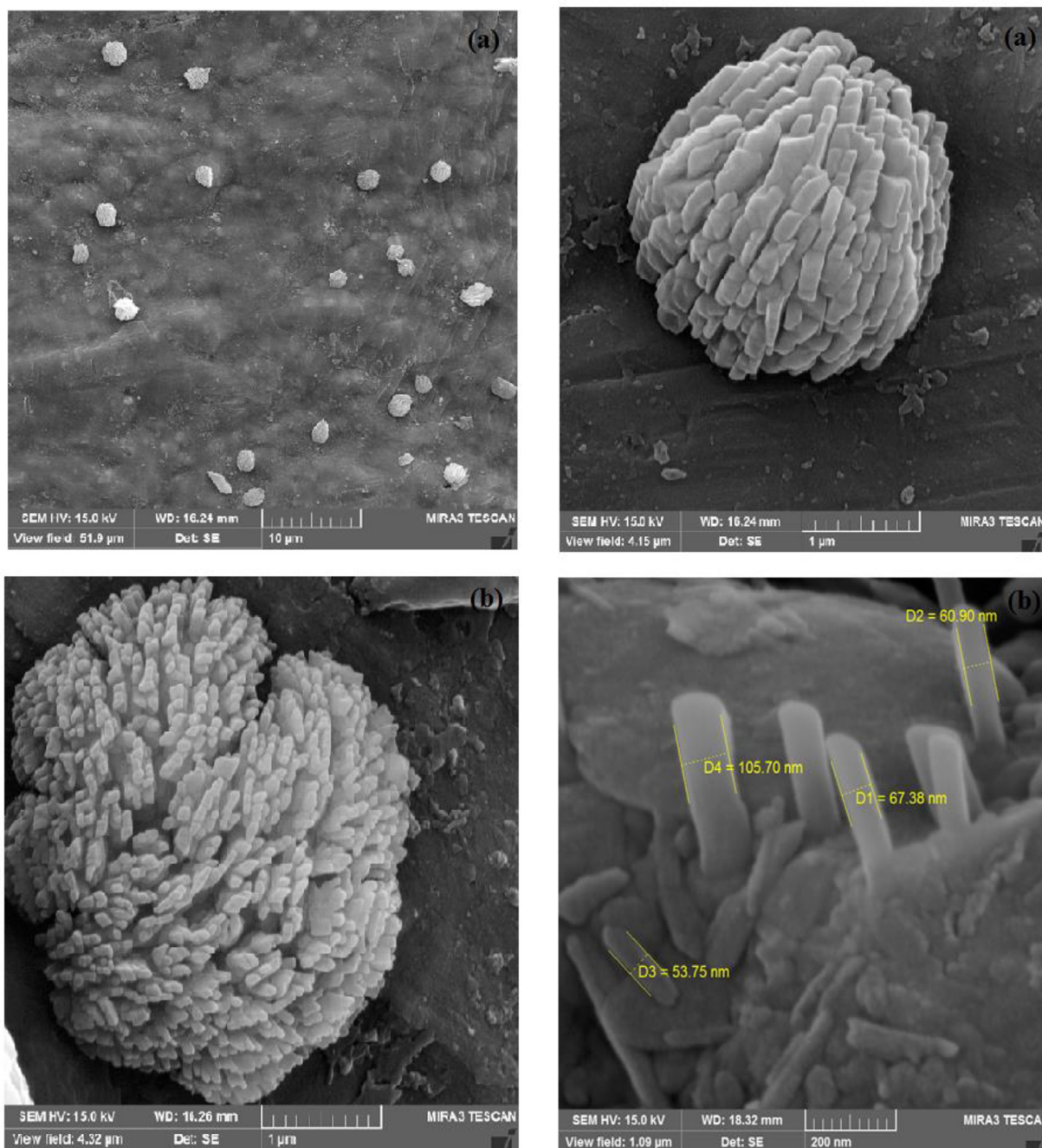


Fig. 6. SEM photograph of nanostructures **C1a** prepared by ultrasonic frequency 80 Hz at concentrations of initial reagents $[\text{Sn(IV)}]/[\text{L}] = 0.01$ mM (a) and 0.007 mM (b).

pair of this atom, $\text{LP}(\text{O}_{\text{P}=\text{O}})$, takes more a p-character. The electronic charge is transferred from the neighbors to the O atom as a result of the polarization effect. This electronic redistribution occurs even more when the ligands are coordinated to SnPh_3Cl , as the polarization effect arises from the electrostatic field of the Sn(IV) atom [40]. For example, the natural electronic configuration (NEC) of the $\text{O}_{\text{P}=\text{O}}$ atom is $[\text{core}] 2s^{1.80} 2p^{5.28}$ in the free ligand (L1), which changes nearly to $[\text{core}] 2s^{1.77} 2p^{5.36}$ by coordinating to the tin in $\text{Sn}(\text{C}_6\text{H}_5)_3\text{ClL1}$. Similarly, the electronic population of 2p orbital of the oxygen increases for the other ligand - complex pairs in Table 2. The hybridization of occupied orbitals by the lone pair of the mentioned atom, as expected, is affected upon complexation. Furthermore, the atomic charges of donor sites become more negative when the ligand is coordinated. Electron delocal-

ization energies, $E^{(2)}$, for the electronic delocalization $\text{LP}(\text{O}_{\text{P}=\text{O}})$ to $\text{LP}^*(\text{Sn})$ (LP^* = empty valence orbital), can be used to characterize the strength of the donor-acceptor coordination interactions. Based on the results in Table 2 for the coordination bond in the complex **C1** containing PhNH and pentamethylene substituents, the higher stabilizing energy of $29.5 \text{ kcal}\cdot\text{mol}^{-1}$ indicates the stronger Sn-O interaction than in the other complexes ($E^{(2)}$: 24.77 (**C2**) and 26.28 (**C3**) $\text{ kcal}\cdot\text{mol}^{-1}$). Another factor in probing the bond strength is the Wiberg bond index. Table 2 shows the selected bond indexes for the complexes. In **C1**, the calculated Wiberg bond order for Sn-O bond is larger than those found for **C2** and **C3**, which demonstrates the stronger donor-acceptor interaction between the central metal and the O atom of the phosphoric triamide moiety.

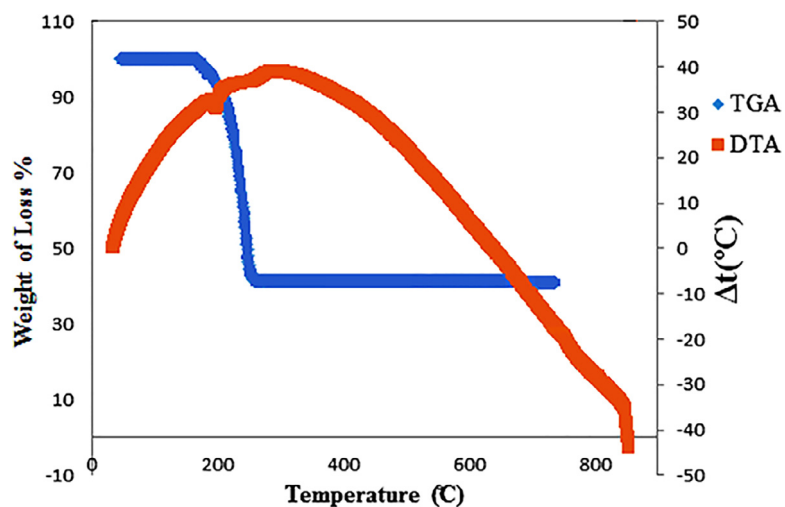


Fig. 7. (a) Thermal behavior (TGA/DTA) and (b) DSC curve of nanostructures C1a.

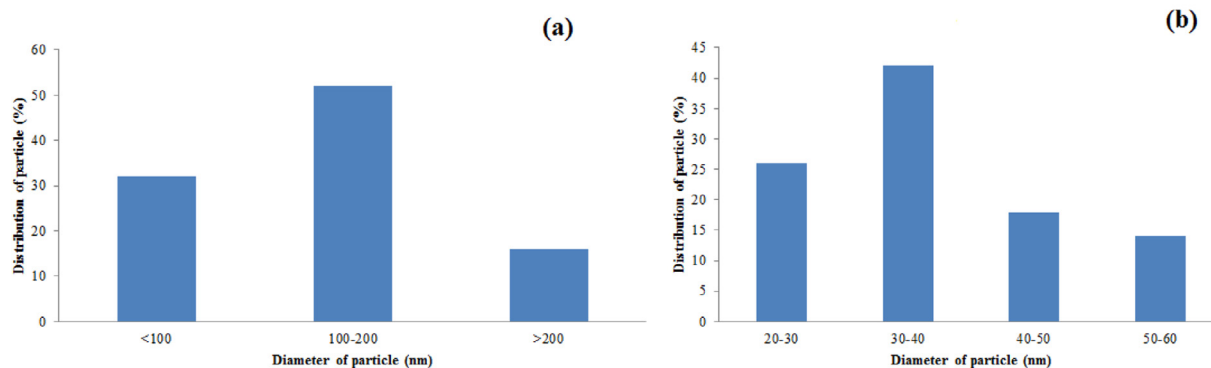
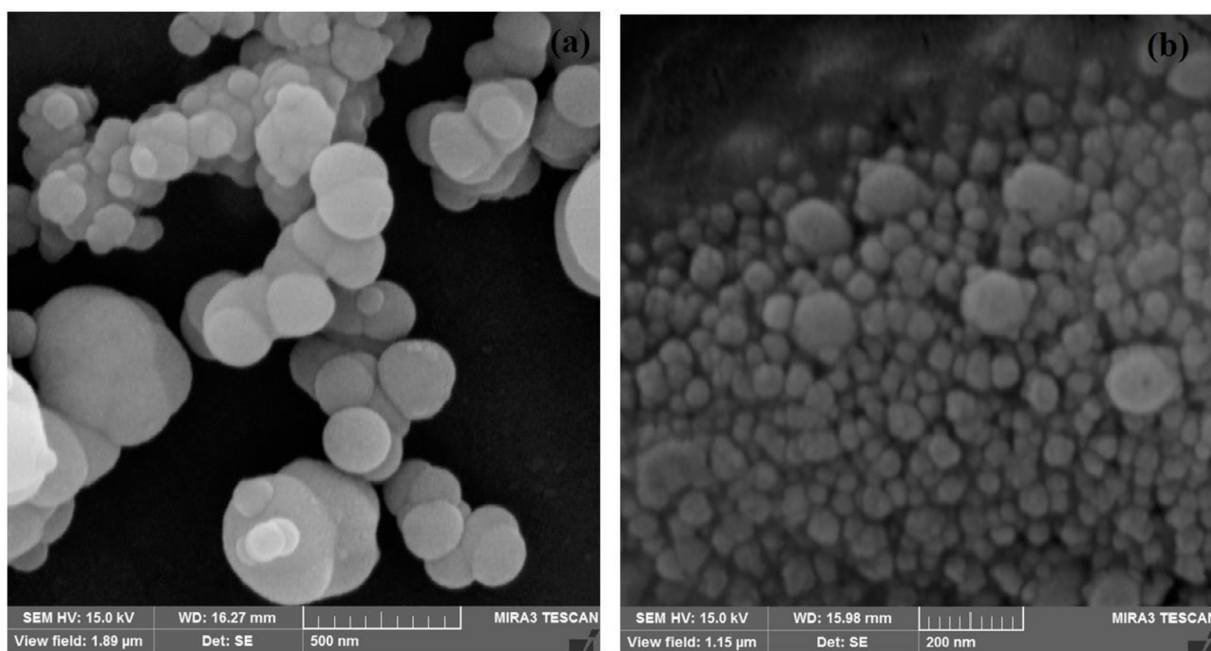


Fig. 8. SEM photograph and the corresponding particle size distribution histogram of SnP_2O_7 nano-particles prepared by calcination of (a) bulk-form C1 and nano-scale C1a (b). (For interpretation of the references to colour in this figure legend, the reader is referred to the web version of this article.)

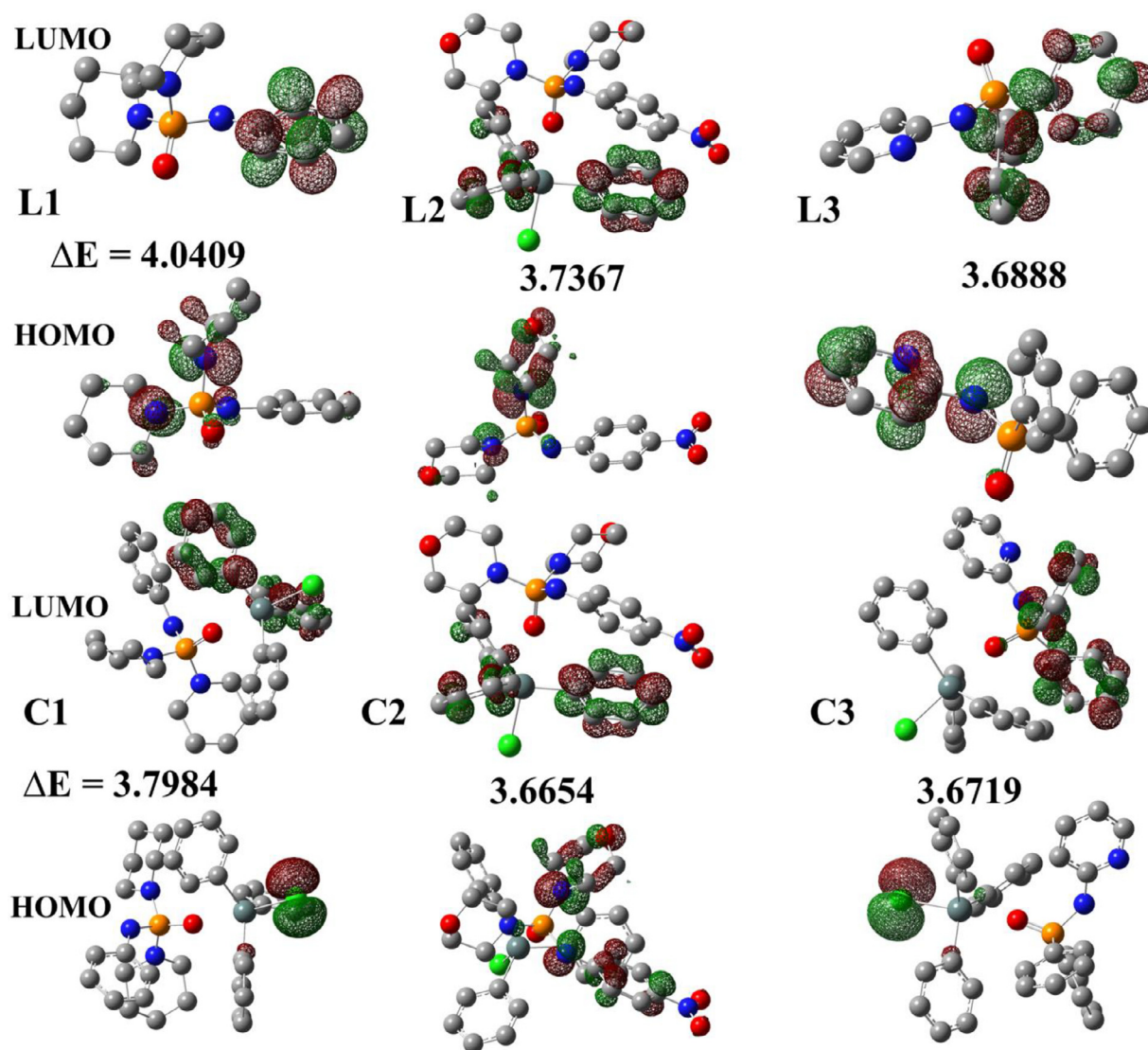


Fig. 9. Plots of the HOMO, LUMO orbitals of the compounds **L1-L3** and **C1-C3**, and ΔE (The energy gap between HOMO and LUMO) (eV).

Table 3

Calculated QTAIM parameters (electron density, ρ , its Laplacian, $\nabla^2 \rho$, and total electronic energy density, $H(r)$) at selected critical points.

H(r)	G(r)	V(r)	Sn...O $\nabla^2 \rho$	P	H(r)	G(r)	P=O V(r)	$\nabla^2 \rho$	ρ	Comp.
-	-	-	-	-	-0.6134	0.5255	-1.1389	-0.3514	0.2309	L1
-	-	-	-	-	-0.6201	0.5311	-1.1512	-0.3559	0.2321	L2
-	-	-	-	-	-0.5950	0.5098	-1.1048	-0.3408	0.2265	L3
-0.1510	0.1608	-0.3118	0.0390	0.1921	-0.5443	0.4736	-1.0179	-0.2829	0.2246	[Sn(C ₆ H ₅) ₃ CIL1] (C1)
-0.1498	0.1528	-0.3026	0.0128	0.1756	-0.5556	0.4845	-1.0400	-0.2844	0.2299	[Sn(C ₆ H ₅) ₃ CIL2] (C2)
-0.1436	0.15495	-0.2986	0.0453	0.1899	-0.5252	0.4556	-0.9808	-0.2784	0.2167	[Sn(C ₆ H ₅) ₃ CIL3] (C3)

3.3. Topological analysis of electron density

The calculated values of the electron density (ρ), its Laplacian ($\nabla^2 \rho$), and electronic energy density $H(r)$ at the bond critical points (BCP) of P=O and Sn-L paths are listed in Table 3. The ρ values at the P=O BCPs are in the range of 0.217–0.232 au and the corresponding $\nabla^2 \rho$ values are all negative, ranging from -0.278 to -0.356 au. Based on the obtained BCPs for P=O in all selected molecules ($\nabla^2 \rho < 0$ and $H(r) < 0$), this bond is the stronger covalent bond in ligand **L2** and its corresponding complex **C2** than in other ligands and complexes (Table 3). Moreover, the electron density (ρ) values at the Sn-L BCPs are in the range of 0.176–0.192 au and the corresponding $\nabla^2 \rho$ values are all positive, ranging from $+0.013$ to

$+0.045$ au, which characterizes the predominantly closed-shell interactions [30]. Despite falling in a region of charge depletion with $\nabla^2 \rho > 0$, the negative values of $H(r)$ suggest that the interactions are principally electrostatic in nature with an amount of tin-ligand covalent interaction. The related ρ and $\nabla^2 \rho$ are larger as the interaction becomes stronger. The trend observed for the Sn-L bonding strength in complexes is in agreement with NBO analysis.

3.4. HOMO and LUMO

The energies of the highest occupied molecular orbital (HOMO) and the lowest unoccupied molecular orbital (LUMO) were computed using a DFT approach [41]. The energy gap, ΔE ($\Delta E = E_{\text{LUMO}}$

- E_{HOMO}), is an important parameter to measure the reactivities of selected molecules (**L1** - **L3**; **C1** - **C3**). Fig. 9 shows the energy gap and isodensity surface plot of HOMO and LUMO for ligands (**L1** - **L3**) and the corresponding triorganotin(IV) complexes (**C1** - **C3**). The ΔE values infer that triorganotin(IV) **C2** has high chemical activity, low kinetic stability and high softness value [42]. As can be seen, the LUMO electrons are mainly delocalized over the phenyl rings for all molecules, except phosphoramidate **L2** with delocalization on nitroaniline moiety. For the most compounds, the HOMO electrons are delocalized over moieties containing nitrogen atom as morpholine, pyridine, and amine rings, as well as Cl atom in two triorganotin(IV) **C1**, **C3** only. Using HOMO and LUMO energies, ionization potential (IP) and electron affinity (EA) can be estimated as $IP \sim -E_{\text{HOMO}}$, $EA \sim -E_{\text{LUMO}}$ [43]. The chemical hardness (η) = $(IP - EA)/2$ [44], electronegativity (χ) = $(IP + EA)/2$ [45], chemical potential (μ) = $(IP + EA)/2$ and chemical softness (S) = $1/2\eta$ [46] values were calculated and were presented in Table S3. According to the information of Table S4, the complex **C1** shows a higher amount of gap energy and hardness (η), while the **C2** is softer than other two complexes. The variation of χ values is supported by the electrostatic potential. For the selected molecules, electron will be partially transferred from the one of low χ to that of high χ (electrons flow from high chemical potential to low chemical potential). These observations can be explained by attention to the substitutions of the P(O) group.

4. Conclusion

In this work, the triphenyltin(IV) adduct with a phosphoramidate ligand, $[\text{Sn}(\text{Ph})_3\text{Cl}(\text{L1})]$ (**C1**), $\{\text{L1} = (\text{C}_6\text{H}_5\text{NH})(\text{O})\text{P}(\text{NC}_5\text{H}_{10})_2\}$, is studied in detail. The structural data clearly demonstrate the formation a two-dimensional coordination polymer with five-coordinated tin centers. The one phosphoramidate ligand and a chloro atom act as donor and acceptor of hydrogen bond between two neighboring molecules, respectively, to form infinite 1D chains. 2D supramolecular architectures are generated from one-dimensional coordination chains via H...H interaction between aromatic phenyl units. Hirshfeld surfaces (HS) and the corresponding fingerprint plots have been used for the further investigation of intermolecular interactions in crystal structure of the complex. Further, nano-strawberries of this complex (**C1a**) have been synthesized by sonochemical process and the SEM image of nano-sized particles of the coordination complex shows the perfect morphology of these nano-structures. The FT-IR and XRD analysis confirm the identical structure of the single crystal and the sonication-assisted sample. Nanomaterial of SnP_2O_7 fabricated by direct calcination of synthesized complex as a precursor at nano-scale has smaller size than its bulk form. To elucidate the electronic properties and nature of binding interactions, QTAIM and NBO analyses have been performed for some phosphoramidates and the corresponding triorganotin complexes (**L1** - **L3**; **C1** - **C3**) as well. The obtained results demonstrate that tin-ligand interactions are principally electrostatic, with a partial amount of covalent overlap in the tin adducts with phosphoramidates. The coordination binding energy represents a strong Sn-O interaction for ligand **L1** in comparison with **L2** and **L3**. Besides, HOMO-LUMO energy gap of the studied triorganotin(IV) adducts indicates importance of the coordinated substituents to P(O) group on the electronic characters.

Credit author statement

Mahtab Alipour: Investigation, Niloufar Dorosti: Supervision, Conceptualization, Maciej Kubicki: Crystallographer & Software, Writing - Review & Editing

Supplementary data

CCDC 1871142 contains the supplementary crystallographic data for $\text{C}_{34}\text{H}_{41}\text{ClN}_3\text{OPSn}$. The data can be obtained free of charge from the Cambridge Crystallographic Data Centre via fax: +441223336033; E-mail: deposit@ccdc.cam.ac.uk or www.ccdc.cam.ac.uk.

Declaration of Competing Interest

The authors declare that they have no known competing financial interests or personal relationships that could have appeared to influence the work reported in this paper

Acknowledgment

Financial support of this work by Lorestan University is gratefully acknowledged.

Supplementary materials

Supplementary material associated with this article can be found, in the online version, at doi:10.1016/j.molstruc.2020.129630.

References

- [1] (a) Z.A.K. Khattak, H.A. Younus, N. Ahmad, B. Yu, H. Ullah, S. Suleman, A.H. Chughtai, B. Moosavi, C. Sombon, F. Verpoort, Mono- and dinuclear organotin(IV) complexes for solvent free cycloaddition of CO₂ to epoxides at ambient pressure, *J. CO₂ Util* 28 (2018) 313–318; (b) M. Tariq, N. Muhammad, M. Sirajuddin, S. Ali, N. AliShah, N. Khalid, M. NawazTahir, M. Rashid-Khan, Synthesis, spectroscopic characterization, X-ray structures, biological screenings, DNA interaction study and catalytic activity of organotin(IV) 3-(4-fluorophenyl)-2-methylacrylic acid derivatives, *J. Organomet. Chem.* 723 (2013) 79–89.
- [2] (a) Z-F. Chen, Y. Peng, Y-Q. Gu, Y-C. Liu, M. Liu, K-B. Huang, K. Hu, H. Liang, High antitumor activity of 5,7-dihalo-8-quinolinolato tin(IV) complexes, *Eur. J. Med. Chem.* 62 (2013) 51–58; (b) M. Hong, H. Yin, X. Zhang, C. Li, C. Yue, S. Cheng, Di- and tri-organotin(IV) complexes with 2-hydroxy-1-naphthaldehyde 5-chloro-2-hydroxybenzoylhydrazone: Synthesis, characterization and in vitro antitumor activities, *J. Organomet. Chem.* 724 (2013) 23–31.
- [3] (a) B. Gleeson, J. Claffey, D. Ertler, M. Hogan, H. Müller-Bunz, F. Paradisi, D. Wallis, M. Tacke, Novel organotin antibacterial and anticancer drugs, *Polyhedron* 27 (2008) 3619–3624; (b) Z-ur Rehman, N. Muhammad, S. Shuja, S. Ali, I.S. Butler, A. Meetsma, M. Khan, New dimeric, trimeric and supramolecular organotin(IV) dithiocarboxylates: Synthesis, structural characterization and biocidal activities, *Polyhedron* 28 (2009) 3439–3448.
- [4] Y. Hu, J. Zhang, Z. Li, T. Li, Crystal structure, Z-scan measurements and theoretical calculations of third-order nonlinear optical properties of tetrachloro(1,10-phenanthroline-N,N')tin(IV), *Synth. Met.* 197 (2014) 194–197.
- [5] K. Gholivand, S. Farshadian, Synthesis and molecular structure of the all-trans- and the trans-cis-isomers of dichlorodimethyltin complexes of phosphoric triamides, *Inorg. Chim. Acta* 368 (2011) 111–123.
- [6] K. Gholivand, R. Salami, Z. Shahsavari, E. Torabi, Novel binuclear and polymeric diorganotin (IV) complexes with N-nicotinyl phosphoramidates: Synthesis, characterization, structural studies and anticancer activity, *J. Organomet. Chem.* 819 (2016) 155–165.
- [7] K. Gholivand, S. Farshadian, Z. Hosseini, K. Khajeh, N. Akbari, Two novel diorganotin phosphonic diamides: syntheses, crystal structures, spectral properties and in vitro antibacterial studies, *Appl. Organomet.Chem.* 24 (2010) 700–707.
- [8] K. Gholivand, M. Rajabi, N. Dorosti, F. Molaei, Synthesis, structural characterization, density functional theory calculations and biological evaluation of a new organotin(IV) complex containing N-isonicotinyl-N',N''-diaryl phosphoric-triamide as N-donor ligand, *Appl. Organomet. chem.* 29 (2015) 739–745.
- [9] M.Eini Roumiani, N. Dorosti, Sonochemical synthesis of a nanodandelion tin(IV) complex with carbacylamidophosphate ligand as anti-Alzheimer agent: Molecular docking study, *Ultrason. Sonochem.* 55 (2019) 207.
- [10] S. Assefa, F. Xia, Y.A. Vlasov, Reinventing germanium avalanche photodetector for nanophotonic on-chip optical interconnects, *Nature* 464 (2010) 80–84.
- [11] N. Melosh, A. Boukai, F. Diana, B. Gerardot, A. Badolato, P. Petroff, J.R. Heath, *Science* 300 (2003) 112–115.
- [12] F. Novio, J. Simmchen, N. Vázquez-Mera, L. Amorín-Ferré, D. Ruiz-Molina, Coordination polymer nanoparticles in medicine, *Coord. Chem. Rev* 257 (2013) 2839–2847.
- [13] (a) K.J. Sankaran, S. Kunuku, B. Sundaravel, P-Y Hsieh, H-C Chen, K-C Leou, N-H Tai, I-N Lin, Gold nanoparticle-ultranano-crystalline diamond hybrid structured materials for highperformance optoelectronic device applications,

- Nanoscale 7 (2015) 4377–4385; (b) D.V. Talapin, J.-S. Lee, M.V. Kovalenko, E.V. Shevchenko, Prospects of Colloidal Nanocrystals for Electronic and Optoelectronic Applications, *Chem. Rev.* 110 (2010) 389–458.
- [14] (a) S.M. Sheta, S.M. El-Sheikh, M.M. Abd-Elzاهر, A.R. Wassel, A novel nano-size lanthanum metal-organic framework based on 5-amino-isophthalic acid and phenylenediamine: Photoluminescence study and sensing applications, *Appl. Organomet. Chem.* 33 (2019) e4777; (b) S. Geranmayeh, M. Mohammadnejad, S. Mohammadi, Sonochemical synthesis and characterization of a new nano Ce(III) coordination supramolecular compound; highly sensitive direct fluorescent sensor for Cu²⁺, *Ultrason. Sonochem.* 40 (2018) 453–459.
- [15] A.M. Kaczmarek, S. Abednatanzi, D. Esquivel, C. Krishnaraj, H. Sekharjena, G. Wang, K. Leus, R. Van Deun, F.J. Romero-Salguero, P. Van Der Voort, Amine-containing (nano-) Periodic Mesoporous Organosilica and its application in catalysis, sorption and luminescence, *Micropor. Mesopor. Mat.* 291 (2020) 109687.
- [16] P.C. Ray, Size and Shape Dependent Second Order Nonlinear Optical Properties of Nanomaterials and Their Application in Biological and Chemical Sensing, *Chem. Rev.* 110 (2010) 5332–5365.
- [17] S. Nikpour, N. Dorosti, F. Afshar, M. Kubicki, Nano- and micro-structure tin (IV) complexes bearing 4-pyridinecarbonylamidophosphate: Sonochemical synthesis, crystal structure, anti-cholinesterase activity, and docking studies, *Appl. Organomet. Chem.* (2020) e5724.
- [18] Y. Jin, B. Lee, T. Hibino, Development and application of SnP207-based proton conductors to intermediate-temperature fuel cells, *J. Jpn. Petrol. Inst.* 53 (1) (2010) 12–23.
- [19] K. Genzaki, P. Heo, M. Sano, T. Hibino, Proton Conductivity and Solid Acidity of Mg-, In-, and Al-Doped SnP207, *J. Electrochem. Soc.* 156 (7) (2009) B806–B810.
- [20] (a) J. Xu, Q. Liu, W.Y. Sun, Shape-controlled zinc(II) oxide nanomaterial constructed from three-dimensional zinc(II) coordination complex, *Solid State Sci* 12 (2010) 1575; (b) Y. Hanifehpour, A. Morsali, B. Mirtamizdoust, S.Woo Joo, Sonochemical synthesis of tri-nuclear lead(II)-azido nano rods coordination polymer with 3,4,7,8-tetramethyl-1,10-phenanthroline (tmph): Crystal structure determination and preparation of nano lead(II)oxide, *J. Mol. Struct.* 1079 (2015) 67–73.
- [21] N. Dorosti, H. Mohammadpour, Synthesis, characterization and biological evaluation of a nanorod five-coordinated Sn(IV) complex. Theoretical studies of (CH₃)₂Sn(O₂PPh₂)₂, *Appl. Organomet. Chem.* (2018) e4610.
- [22] F. Bigdeli, A. Morsali, Pascal Retailleau, Syntheses and characterization of different zinc(II) oxide nano-structures from direct thermal decomposition of 1D coordination polymers, *Polyhedron* 29 (2010) 801–806.
- [23] K. Gholivand, H.R. Mahzouni, Electronic and steric effects of substituents on the conformational diversity and hydrogen bonding of N-(4-X-phenyl)-N,N'-bis(piperidinyl) phosphoric triamides (X = F, Cl, Br, H, CH₃): A combined experimental and DFT study, *Polyhedron* 30 (2011) 61–69.
- [24] Agilent TechnologiesCrysAlis PRO (Version 1.171.33.36d), Agilent Technologies Ltd, 2011.
- [25] a) G.M. Sheldrick, *Acta Crystallogr* (2015) A71, 3–8; b) G.M. Sheldrick, *Acta Crystallogr* (2015) C71, 3–8.
- [26] a) S. K. Wolff, D. J. Grimwood, J. J. McKinnon, M. J. Turner, D. Jayatilaka, M. A. Spackman, *Crystalexplorer 3.0*, University of Western Australia, Perth, Australia, 2012.; b) M.A. Spackman, J.J. McKinnon, Fingerprinting intermolecular interactions in molecular crystals, *Cryst. Eng. Comm.* 4 (2002) 378–392.
- [27] M.J. Frisch, et al., *Gaussian* (2010) 09 Revision B.01, Gaussian, Inc., Wallingford, CT.
- [28] (a) P.J. Stephens, F.J. Devlin, C.F. Chabalowski, M.J. Frisch, Ab Initio Calculation of Vibrational Absorption and Circular Dichroism Spectra Using Density Functional Force Fields, *J. Phys. Chem.* 98 (1994) 11623–11627; (b) A.D. Becke, Density-functional thermochemistry. III. The role of exact exchange, *J. Chem. Phys.* 98 (1993) 5648–5652.
- [29] P.J. Hay, W.R. Wadt, Ab initio effective core potentials for molecular calculations. Potentials for K to Au including the outermost core orbitals, *J. Chem. Phys.* 82 (1985) 299–310.
- [30] a) R. F. W. Bader, *Atoms in Molecules - A Quantum Theory*, Oxford University Press, New York, 1990.; (b) R.F.W. Bader, A quantum theory of molecular structure and its applications, *Chem. Rev.* 91 (1991) 893–928.
- [31] A.E. Reed, L.A. Curtiss, F. Weinhold, Intermolecular interaction from a natural bond orbital, donor-acceptor view point, *Chem. Rev.* 88 (1988) 899.
- [32] A.R. Narga, M. Schuermann, C. Silvestru, Hypervalent organotin(IV) derivatives containing [2-(Me₂NCH₂)C₆H₄]Sn moieties. Competition between nitrogen and chalcogen atoms for coordination to the metal centre, *J. Organomet. Chem.* 623 (2001) 161–167.
- [33] (a) N.W. Alcock, J.F. Sawyer, Secondary bonding. Part 2. Crystal and molecular structures of diethyltin dichloride, dibromide, and di-iodide, *J. Chem. Soc. Dalton Trans.* (1977) 1090–1095; (b) M. Hill, M.F. Mahon, K.C. Molloy, Tris(triorganostannyltetrazoles): synthesis and supramolecular structures, *J. Chem. Soc. Dalton Trans.* (1996) 1857–1865.
- [34] A.R. Corbridge, Phosphorus, an Outline of its Chemistry, Biochemistry and Technology, Elsevier, The Netherlands, 1995 fifth ed..
- [35] Z. Shariatina, H.S. Mirhosseini Mousavi, P.J. Bereciartua, M. Dusek, Structures of a novel phosphoric triamide and its organotin(IV) complex, *J. Organomet. Chem.* (2013) 432–438 745–746.
- [36] K. Gholivand, A. Gholami, S.K. Tizhoush, K.J. Schenk, F. Fadaei, A. Bahrami, Steric and electronic control over the structural diversity of N-(n-pyridinyl) diphenylphosphinic amides (n = 2 and 4) as difunctional ligands in triphenyltin(IV) adducts, *RSC Adv* 4 (2014) 44509–44516.
- [37] J.J. McKinnon, D. Jayatilaka, M.A. Spackman, Towards quantitative analysis of intermolecular interactions with Hirshfeld surfaces, *Chem. Commun.* (2007) 3814–3816.
- [38] S.K. Wolff, D.J. Grimwood, J.J. McKinnon, M.J. Turner, D. Jayatilaka, M.A. Spackman, *CrystalExplorer 3.0*, University of Western Australia, Perth, Australia, 2012.
- [39] N. Dorosti, B. Delfan, M. Khodadadi, Ultrasonic-assisted synthesis and biological evaluation of a nano-rod diorganotin phosphonic diamide: Precursor for the fabrication of SnP207 nano-structure, *Appl. Organomet. Chem.* (2017) e3875.
- [40] K. Gholivand, H.R. Mahzouni, M.D. Esrafil, Structure, bonding, electronic and energy aspects of a new family of early lanthanide (La, Ce and Nd) complexes with phosphoric triamides: Insights from experimental and DFT studies, *Dalton Trans* 41 (2012) 1597.
- [41] M.H. Jamroz, *Vibrational energy distribution analysis, VEDA 4 computer program*, Poland, 2004.
- [42] I. Fleming, *Frontier Orbitals and Organic Chemical Reactions*, John Wiley & Sons, New York, 1976.
- [43] Z. Zhou, H.V. Navangul, Absolute hardness and aromaticity: MNDO study of benzenoid hydrocarbons, *J. Phys. Org. Chem.* 3 (1990) 784–788.
- [44] P. Senet, Chemical hardnesses of atoms and molecules from frontier orbitals, *Chem. Phys. Lett.* 275 (1997) 527.
- [45] L. Pauling, *The Nature of the Chemical Bond*, Cornell University Press, Ithaca, New York, 1960.
- [46] A. Khansari, M. Enhessari, M. Salavati-Niasari, Synthesis and Characterization of Nickel Oxide Nanoparticles from Ni(salen) as Precursor, *J. Cluster Sci.* 24 (2013) 289–297.